



Cite this: DOI: 10.1039/d1cc03460j

Received 29th June 2021,  
Accepted 7th July 2021

DOI: 10.1039/d1cc03460j

rsc.li/chemcomm

# Low-temperature architecture of a cubic-phase CsPbBr<sub>3</sub> single crystal for ultrasensitive weak-light photodetectors†

Xiangfeng Wei,<sup>‡a</sup> Han Liu,<sup>‡a</sup> Zhixiang Zhang,<sup>b</sup> Wenchao Xu,<sup>a</sup> Wenjun Huang,<sup>a</sup>  
Lin-Bao Luo<sup>id</sup>\*<sup>b</sup> and Jiehua Liu<sup>id</sup>\*<sup>ac</sup>

**We present the first report of a water-regulated method for obtaining a cubic-phase CsPbBr<sub>3</sub> single crystal that could be frozen at low temperature with a CsBr/PbBr<sub>2</sub> ratio of 1:1. The cubic CsPbBr<sub>3</sub> single-crystal photodetector exhibits a superior responsivity of 278 A W<sup>-1</sup>, an EQE of 6.63 × 10<sup>4</sup>%, and an ultrahigh detectivity of 4.36 × 10<sup>13</sup> Jones under low-power 520 nm irradiation at 3 V.**

All inorganic perovskite CsPbX<sub>3</sub> (X = I, Br, Cl) materials have been widely used in the field of optoelectronic devices due to better thermal stability than that of organic–inorganic perovskite.<sup>1–3</sup> CsPbX<sub>3</sub> single crystals are suitable for high-performance photoelectric devices because of their intrinsic properties including high light-absorption coefficients, long carrier transport distances, and few defects compared with micro/nanocrystals and polycrystalline films.<sup>4–8</sup> Importantly, single crystals also exhibit orderly crystal planes, anisotropic photoelectric properties, and stability in external environments, which is superior to micro/nanocrystals or thin films.<sup>9,10</sup> CsPbBr<sub>3</sub> single crystals are the most popular in the field of inorganic perovskites.<sup>10,11</sup> CsPbBr<sub>3</sub> has several characteristics including a direct bandgap, narrow emission peaks, wide absorption, high quantum yield and good luminescence performance, which provide it with significant application potential in the fields of light-emitting diodes,<sup>12,13</sup> photoluminescence,<sup>14,15</sup> photoelectric devices,<sup>16,17</sup> and X-ray/gamma-ray detection.<sup>18–20</sup>

There are three phases of CsPbBr<sub>3</sub> crystals: orthorhombic, tetragonal, and cubic structures. Two phase transitions occur at

88 and 131 °C for orthorhombic–tetragonal and tetragonal–cubic transformations, respectively.<sup>21,22</sup> Most of the reported CsPbBr<sub>3</sub> single crystals are orthorhombic structure at room temperature.<sup>7,23</sup> Lattice-dynamics calculations demonstrated that CsPbX<sub>3</sub> perovskites exhibit vibrational instabilities associated with octahedral tilting in their high-temperature cubic phase.<sup>24</sup> Also, the Bridgman method was used to grow high-quality orthorhombic CsPbBr<sub>3</sub> single crystals from the melt but post treatments were required including cutting and polishing.<sup>9</sup> CsPbBr<sub>3</sub> single crystals have been obtained using simple solution methods with CsBr/PbBr<sub>2</sub> ratios of 1:2 or 2:3.<sup>25,26</sup> However, the unequal molar ratios of Cs/Pb in the solution and single crystals cause the coexistence of CsPbBr<sub>3</sub> with Cs<sub>4</sub>PbBr<sub>6</sub> or CsPb<sub>2</sub>Br<sub>5</sub>.<sup>27–29</sup> The main reason is the largely different saturation solubility of CsBr and PbBr<sub>2</sub> in dimethyl sulfoxide (DMSO) solution.

Cubic-phase CsPbBr<sub>3</sub> nanocrystals or quantum dots were successfully synthesized using structure-directing agents, but cubic-phase CsPbBr<sub>3</sub> single crystals have not been reported so far.<sup>30–32</sup> Very recently, density functional theory (DFT) calculation results found that the cubic-phase CsPbBr<sub>3</sub> has smaller surface energy than that of the orthorhombic phase.<sup>33</sup> The desired method is that the 1:1 ratio of CsBr and PbBr<sub>2</sub> as inputs is in proportion to the product (CsPbBr<sub>3</sub>), which is beneficial for the synthesis of high-purity CsPbBr<sub>3</sub> crystals. Herein, we used water as a cosolvent to enhance the saturation solubility of CsBr, while decreasing the saturation solubility of PbBr<sub>2</sub> in the DMSO–H<sub>2</sub>O system. As a result, cubic-phase CsPbBr<sub>3</sub> single crystals are successfully synthesized using the water-regulated method at low temperature. The cubic CsPbBr<sub>3</sub> single-crystal based photodetector exhibits superior responsivity, EQE, and detectivity at under low-power 520 nm irradiation.

We first measured the saturation solubility of CsBr and PbBr<sub>2</sub> in DMSO in the temperature range of 40–70 °C as shown in Fig. 1a. The results show that PbBr<sub>2</sub> becomes more soluble in DMSO when increasing temperature. However, there was no significant change for the saturation solubility of CsBr in DMSO solution. The cosolvent method was used to control an

<sup>a</sup> Future Energy Laboratory, School of Materials Science and Engineering, Hefei University of Technology, Hefei, 230009, China. E-mail: liujh@hfut.edu.cn

<sup>b</sup> School of Electronic Science and Applied Physics, Hefei University of Technology, Hefei, 230009, China. E-mail: luolb@hfut.edu.cn

<sup>c</sup> Key Laboratory of Advanced Functional Materials and Devices of Anhui Province, Engineering Research Center of High Performance Copper Alloy Materials and Processing, Ministry of Education, Hefei, 230009, China

† Electronic supplementary information (ESI) available: Experimental details, saturation solubility curves, XRD patterns, TRPL spectra, Raman spectrum, *I*–*t* curves, and detectivity. See DOI: 10.1039/d1cc03460j

‡ X. Wei and H. Liu contributed equally.

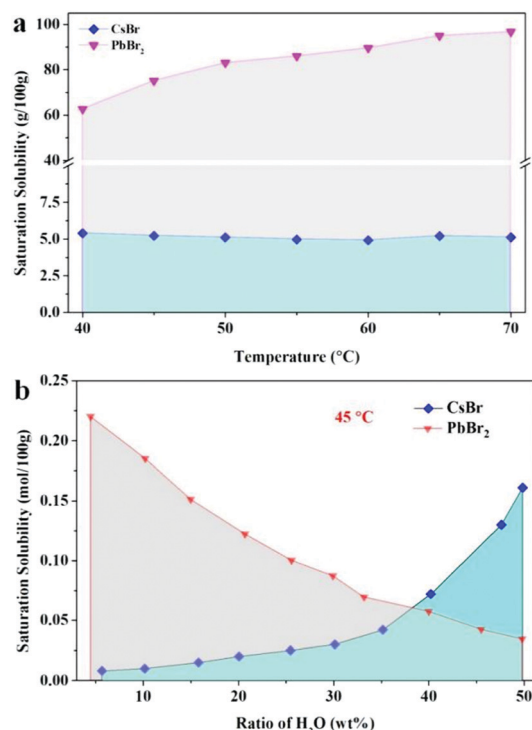


Fig. 1 (a) The saturation solubility curves of CsBr and PbBr<sub>2</sub> in DMSO solution at different temperatures; (b) the saturation solubility curves of CsBr and PbBr<sub>2</sub> in DMSO-H<sub>2</sub>O solution at 45 °C.

appropriate ratio of saturation solubility for inputs in the solvent. To obtain high-purity CsPbBr<sub>3</sub> single crystals, the preferred cosolvent (water) has the following properties including non-ionic agent, stability, and low toxicity. In particular, CsBr has a high solubility of 55 g in 100 g H<sub>2</sub>O at room temperature. A clean and non-ionic cosolvent, adding H<sub>2</sub>O not only increases the saturation solubility of CsBr, but also reduces the saturation solubility of PbBr<sub>2</sub>. We think that high-quality CsPbBr<sub>3</sub> single crystals may be grown when the saturation solubilities of both CsBr and PbBr<sub>2</sub> are close to or equal to each other. Therefore, it is very important to strictly control the amount of H<sub>2</sub>O.

Fig. 1b shows the DMSO-H<sub>2</sub>O solution can be obtained with a molar ratio of 1:1 for CsBr and PbBr<sub>2</sub> at 45 °C when adding 38.1 wt% H<sub>2</sub>O. Table S1 (ESI<sup>†</sup>) shows that less water needs to be added as the temperature rises. To obtain the same saturated solubility for CsBr and PbBr<sub>2</sub>, the amounts of water added are 38.2, 36.8, and 27.2% at 40, 50, and 60 °C. Finally, pure CsPbBr<sub>3</sub> single crystals are successfully synthesized with a Cs/Pb ratio of 1:1 in a 38 wt% H<sub>2</sub>O in H<sub>2</sub>O-DMSO solution using acetonitrile as the antisolvent.

An orange CsPbBr<sub>3</sub> single crystal 2 mm in length was obtained in the above method. The inset of Fig. 2a is a photograph of the CsPbBr<sub>3</sub> single crystal that was obtained in the H<sub>2</sub>O-DMSO solution using acetonitrile as the antisolvent. The XRD pattern of the CsPbBr<sub>3</sub> single crystal is displayed in Fig. 2a. as the as-synthesized CsPbBr<sub>3</sub> single crystal is assigned to the cubic phase (JCPDS card No. 54-0752) rather than the orthorhombic and tetragonal phases. There are typical 2-theta peaks at 15.28°, 30.75°, 46.84°, and 63.98°

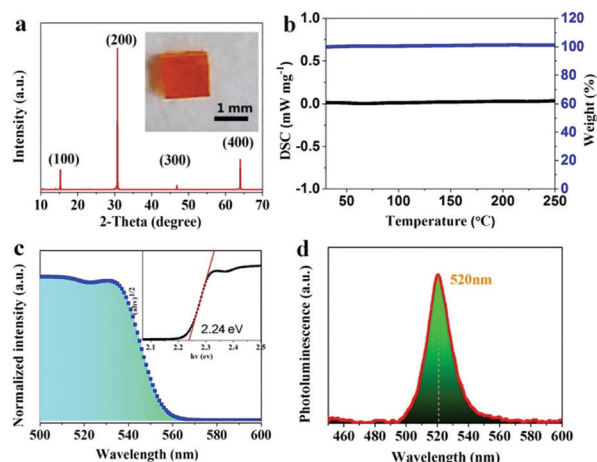


Fig. 2 (a) XRD patterns of the CsPbBr<sub>3</sub> powder and the single crystal and its photograph (inset), (b) DSC and TGA curves, (c) UV-Vis absorption spectrum and Tauc plot (inset), and (d) steady-state PL spectrum of the CsPbBr<sub>3</sub> single crystal.

corresponding to crystal facets of (100), (200), (300), and (400), respectively. The (100) peak centered at 15.28° of the cubic CsPbBr<sub>3</sub> single crystal is larger than 15.15° for the orthorhombic phase, which exhibits smaller lattice parameters to that of the frozen cubic phase obtained at low temperature. The strong peaks indicated that the CsPbBr<sub>3</sub> single crystal has high crystal quality, which is mainly attributed to the preferred orientation of crystal nucleus formation and single-crystal growth of the cubic phase. The XRD pattern of the CsPbBr<sub>3</sub> powder matches the orthorhombic phase (JCPDS card No. 72-7929) (Fig. S2, ESI<sup>†</sup>). A phase change occurs when the cubic-phase single crystal is ground into a powder *via* increased defects and stress induction. We also confirmed that the cubic-phase could exist on freezing with smaller crystal cell parameters (Fig. S3, ESI<sup>†</sup>).

Thermal analysis provides a useful tool to analyze the phase transformations of the CsPbBr<sub>3</sub> crystal. Fig. 2b shows there is no phase change based on its differential scanning calorimetry (DSC) and thermal gravity analysis (TGA) curves from room temperature to 250 °C. This is different from the reported melt-grown CsPbBr<sub>3</sub> crystals that have peaks at 88 and 131 °C for orthorhombic-tetragonal and tetragonal-cubic phase transformations, respectively.<sup>22</sup> The thermal-analysis result is consistent with XRD data for the cubic-phase CsPbBr<sub>3</sub> single crystal. Fig. 2c shows the UV-Vis absorption spectrum of the CsPbBr<sub>3</sub> single crystal with an absorption edge at around 553 nm. The CsPbBr<sub>3</sub> single crystal has a bandgap ( $E_g$ ) of 2.24 eV calculated using the Tauc curve (inset of Fig. 2c) that is close to the reported value.<sup>26,34</sup>

Steady-state and time-resolved steady-state photoluminescence (PL and TRPL) spectra were used to investigate the photoluminescence performance of CsPbBr<sub>3</sub> single crystals with an excitation wavelength of 490 nm. The cubic-phase CsPbBr<sub>3</sub> single crystal has a PL emission peak centered at 520 nm (Fig. 2d) and the average carrier lifetime ( $\tau_{av}$ ) is 1.48 ns (Fig. S4, ESI<sup>†</sup>), which is longer than that of nanoparticles with rich defects.<sup>35</sup> The results suggest the photogenerated electron is extracted more efficiently for CsPbBr<sub>3</sub> single crystals than that of nanoparticles or polycrystalline films.

Fig. S5 (ESI†) shows the Raman spectrum of the CsPbBr<sub>3</sub> single crystal and provides the vibrational modes of the Pb–Br framework excited using a red laser at 633 nm at room temperature. There are three Raman-active modes for the CsPbBr<sub>3</sub> crystal at 72.4, 127.2, and 311.9 cm<sup>−1</sup> for the Pb–Br vibrational mode, the motion of the Cs<sup>+</sup> cations, and the second-order phonon mode of the Pb–Br framework, respectively.

The cubic CsPbBr<sub>3</sub> single crystals were used in photodetectors with a Au–CsPbBr<sub>3</sub>–Au structure based on a high-quality crystal interface. The schematic diagram of the CsPbBr<sub>3</sub> photodetector is shown in Fig. 3a. The details of fabrication are provided in the ESI.† Fig. 3b shows an FESEM image of the device with the actual width of 14 μm between both Au electrodes. According to the bandgap of CsPbBr<sub>3</sub>, we choose 520 nm light with low-power intensities of 0.724–13.48 μW cm<sup>−2</sup>. We focused on low-power illumination to ensure light absorption on the surface of the CsPbBr<sub>3</sub> single crystal.

Fig. 3c shows the current–voltage (*I*–*V*) plots of the single-crystal photodetector measured in the dark and under illumination with different light intensities. The dark current is only 0.035 μA at 3 V. The current increases to 0.26 μA at 3 V, when the light densities increase from 0 to 13.48 μW cm<sup>−2</sup>, indicating the modulation effect of light intensity on the photocurrent. Fig. S6 (ESI†) shows that the photocurrent changes with biases from 1–9 V under the illumination of 12.02 μW cm<sup>−2</sup> for the CsPbBr<sub>3</sub> single-crystal photodetector. The photocurrents are 0.49, 2.60, 4.29, 6.44, and 9.57 μA at biases of 1, 3, 5, 7, 9 V, respectively. The photocurrents increase linearly with the increase of biases, indicating the detector has good high-voltage sensitivity and high responsiveness.

Therefore, we further determined the responsivity (*R*), external quantum efficiency (EQE), and detectivity (*D*\*) to investigate

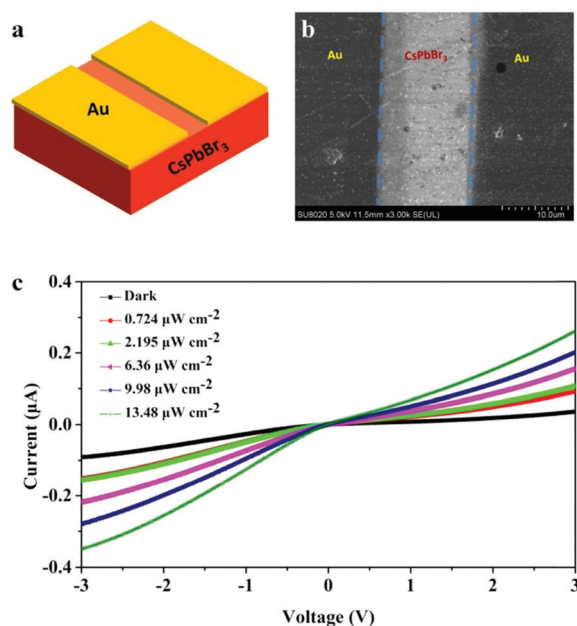


Fig. 3 (a) Schematic diagram, (b) FESEM image, and (c) *I*–*V* curves of the cubic-phase CsPbBr<sub>3</sub> single-crystal photodetector with 0.724–13.48 μW cm<sup>−2</sup> at 3 V.

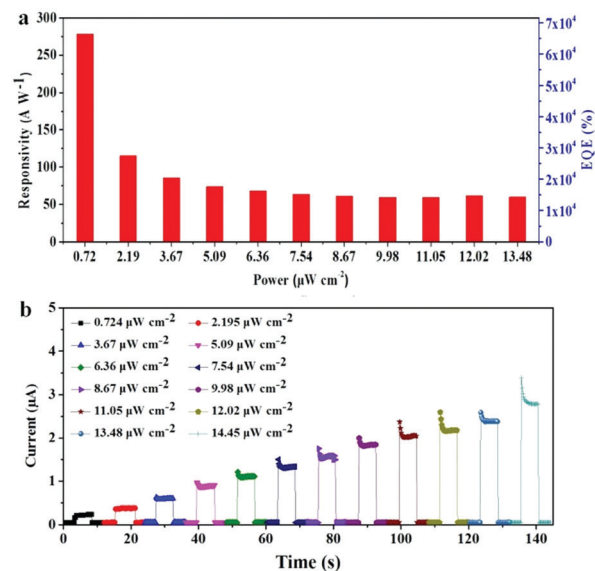


Fig. 4 (a) *R* and EQEs, and (b) Time-dependent photocurrents with on–off cycles under irradiation of 520 nm with varying light intensities from 0.724 to 14.45 μW cm<sup>−2</sup>.

the photoelectric performance of the photodetector. Responsivity represents the ratio of photon-excited current to irradiation flux. EQEs can be obtained from responsivity to evaluate the photocurrent conversion ability of devices by changing the ratio of current/incident light power to electron quantity/photon quantity. *D*\*) is used to characterize the sensitivity of the photodetector. The details are provided in the ESI.†

Fig. 4a shows the histograms of *R* and EQEs for single-crystal photodetector under irradiation of 520 nm with varying light intensities from 0.724 to 13.48 μW cm<sup>−2</sup>. Interestingly, there an ultrahigh *R* of 278 A W<sup>−1</sup> and EQE of 6.64 × 10<sup>4</sup>% under low-power irradiation of 0.724 μW cm<sup>−2</sup> was observed. The results show that the *R* and EQEs obviously reduce with enhanced power from 0.72–5.09 μW cm<sup>−2</sup>. However, they reduce slowly when the power is enhanced to 7.54 μW cm<sup>−2</sup>. The performance of the device is one of the best results compared with previous works on CsPbX<sub>3</sub>-based photodetectors as shown in Table S2 (ESI†). The result is close to microconcave MAPbBr<sub>3</sub> single-crystal photodetectors.<sup>1</sup>

Fig. S7 (ESI†) shows a high *D*\*) of above 4.36 × 10<sup>13</sup> Jones is obtained from the cubic-phase single-crystal photodetector under a low-power irradiation of 0.724 μW cm<sup>−2</sup>. The weak-light photocurrent still increases when enhancing the light intensity, indicating that the device exhibits excellent photoelectric performance for weak light. Fig. 4b shows the curve of time-dependent photocurrents with on–off cycles under irradiation of 520 nm. The photocurrent increases in a near-linear trend with the increase of light power to 3 V. The photocurrent increases linearly with light intensity.

In summary, cubic-phase CsPbBr<sub>3</sub> bulk crystals, which are stable on freezing with smaller crystal cell parameters at room temperature, were successfully synthesized at low temperature using the water-regulated growth method for the first time. The temperature of crystal growth was 45 °C with a 1 : 1 ratio of

CsBr–PbBr<sub>2</sub> in DMSO and H<sub>2</sub>O mixed solvents. The cubic phase has smaller lattice parameters indicating the possibility of cubic CsPbBr<sub>3</sub> bulk crystals. In the mixed solution, the controllable processes are obtained by regulating the ratios of DMSO and H<sub>2</sub>O and the temperature of crystal growth. The cubic CsPbBr<sub>3</sub> single-crystal based photodetector exhibits ultra-sensitive weak-light photoelectric properties including responsivity, EQEs, and detectivity under low-power irradiation of 520 nm. More importantly, this is a universal strategy for designing a low-temperature method for inorganic CsPbX<sub>3</sub> single crystals (Fig. S8, ESI†).

This research was supported by the National Natural Science Foundation of China (U1832136, 21303038, and 62074048) and the Fundamental Research Funds for the Central Universities (JZ2020HGQA0149).

## Conflicts of interest

There are no conflicts to declare.

## Notes and references

- H. Liu, X. Wei, Z. Zhang, X. Lei, W. Xu, L. Luo, H. Zeng, R. Lu and J. Liu, *J. Phys. Chem. Lett.*, 2019, **10**, 786–792.
- S. D. Stranks and H. J. Snaith, *Nat. Nanotechnol.*, 2015, **10**, 391–402.
- D. Shi, V. Adinolfi, R. Comin, M. J. Yuan, E. Alarousu, A. Buin, Y. Chen, S. Hoogland, A. Rothenberger, K. Katsiev, Y. Losovyj, X. Zhang, P. A. Dowben, O. F. Mohammed, E. H. Sargent and O. M. Bakr, *Science*, 2015, **347**, 519–522.
- J. R. Zhang, G. Hodes, Z. W. Jin and S. Z. Liu, *Angew. Chem., Int. Ed.*, 2019, **58**, 15596–15618.
- M. N. Liu, H. C. Zhang, D. Gedamu, P. Fourmont, H. Rekola, A. Hiltunen, S. G. Cloutier, R. Nechache, A. Priimagi and P. Vivo, *Small*, 2019, **15**, 1900801.
- H. F. Gao, J. G. Feng, Y. Y. Pi, Z. H. Zhou, B. Zhang, Y. C. Wu, X. D. Wang, X. Y. Jiang and L. Jiang, *Adv. Funct. Mater.*, 2018, **28**, 1804349.
- Y. F. Wang, F. Yang, X. Z. Li, F. Ru, P. Liu, L. Wang, W. Ji, J. Xia and X. M. Meng, *Adv. Funct. Mater.*, 2019, **29**, 1904913.
- P. B. Gui, H. Zhou, F. Yao, Z. H. Song, B. R. Li and G. J. Fang, *Small*, 2019, **15**, 1902618.
- P. Zhang, G. Zhang, L. Liu, D. Ju, L. Zhang, K. Cheng and X. Tao, *J. Phys. Chem. Lett.*, 2018, **9**, 5040–5046.
- M. I. Saidaminov, M. A. Haque, J. Almutlaq, S. Sarmah, X. H. Miao, R. Begum, A. A. Zhumekenov, I. Dursun, N. Cho, B. Murali, O. F. Mohammed, T. Wu and O. M. Bakr, *Adv. Opt. Mater.*, 2017, **5**, 1600704.
- J. X. Yu, G. X. Liu, C. M. Chen, Y. Li, M. R. Xu, T. L. Wang, G. Zhao and L. Zhang, *J. Mater. Chem. C*, 2020, **8**, 6326–6341.
- C. Chen, T. Han, S. Tan, J. J. Xue, Y. P. Zhao, Y. F. Liu, H. R. Wang, W. Hu, C. Bao, M. Mazzeo, R. Wang, Y. Duan and Y. Yang, *Nano Lett.*, 2020, **20**, 4673–4680.
- Y. Shen, M. N. Li, Y. Q. Li, F. M. Xie, H. Y. Wu, G. H. Zhang, L. Chen, S. T. Lee and J. X. Tang, *ACS Nano*, 2020, **14**, 6107–6116.
- T. Ahmed, S. Seth and A. Samanta, *ACS Nano*, 2019, **13**, 13537–13544.
- V. I. Yudin, M. S. Lozhkin, A. V. Shurukhina, A. V. Emeline and Y. V. Kapitonov, *J. Phys. Chem. C*, 2019, **123**, 21130–21134.
- G. Q. Tong, T. T. Chen, H. Li, L. B. Qiu, Z. H. Liu, Y. Y. Dang, W. T. Song, L. K. Ono, Y. Jiang and Y. B. Qi, *Nano Energy*, 2019, **65**, 104015.
- H. W. Yuan, Y. Y. Zhao, J. L. Duan, Y. D. Wang, X. Y. Yang and Q. W. Tang, *J. Mater. Chem. A*, 2018, **6**, 24324–24329.
- Y. H. He, L. Matei, H. J. Jung, K. M. McCall, M. Chen, C. C. Stoumpos, Z. F. Liu, J. A. Peters, D. Y. Chung, B. W. Wessels, M. R. Wasielewski, V. P. Dravid, A. Burger and M. G. Kanatzidis, *Nat. Commun.*, 2018, **9**, 1609.
- W. C. Pan, B. Yang, G. D. Niu, K. H. Xue, X. Y. Du, L. X. Yin, M. Y. Zhang, H. D. Wu, X. S. Miao and J. Tang, *Adv. Mater.*, 2019, **31**, 1904405.
- W. Z. Wang, H. Meng, H. Z. Qi, H. T. Xu, W. B. Du, Y. H. Yang, Y. S. Yi, S. Q. Jing, S. H. Xu, F. Hong, J. Qin, J. Huang, Z. Xu, Y. Y. Zhu, R. Xu, J. M. Lai, F. Xu, L. J. Wang and J. T. Zhu, *Adv. Mater.*, 2020, **45**, 2001540.
- S. Hirotsu, J. Harada, M. Iizumi and K. Gesi, *J. Phys. Soc. Jpn.*, 1974, **37**, 1393–1398.
- M. Rodova, J. Brozek, K. Knizek and K. Nitsch, *J. Therm. Anal. Calorim.*, 2003, **71**, 667–673.
- X. Zhang, X. Bai, H. Wu, X. Zhang, C. Sun, Y. Zhang, W. Zhang, W. Zheng, W. W. Yu and A. L. Rogach, *Angew. Chem., Int. Ed.*, 2018, **57**, 3337–3342.
- R. X. Yang, J. M. Skelton, E. L. da Silva, J. M. Frost and A. Walsh, *J. Phys. Chem. Lett.*, 2017, **8**, 4720–4726.
- D. N. Dirin, I. Cherniukh, S. Yakunin, Y. Shynkarenko and M. V. Kovalenko, *Chem. Mater.*, 2016, **28**, 8470–8474.
- H. J. Zhang, X. Liu, J. P. Dong, H. Yu, C. Zhou, B. B. Zhang, Y. D. Xu and W. Q. Jie, *Cryst. Growth Des.*, 2017, **17**, 6426–6431.
- P. Acharyya, P. Pal, P. K. Samanta, A. Sarkar, S. K. Pati and K. Biswas, *Nanoscale*, 2019, **11**, 4001–4007.
- J. W. Xu, W. X. Huang, P. Y. Li, D. R. Onken, C. C. Dun, Y. Guo, K. B. Ucer, C. Lu, H. Z. Wang, S. M. Geyer, R. T. Williams and D. L. Carroll, *Adv. Mater.*, 2017, **29**, 1703703.
- X. F. Wei, J. H. Liu, H. Liu, X. Y. Le, H. S. Qian, H. L. Zeng, F. C. Meng and W. Q. Deng, *Inorg. Chem.*, 2019, **58**, 10620–10624.
- J. Liu, K. Song, Y. Shin, X. Liu, J. Chen, K. X. Yao, J. Pan, C. Yang, J. Yin, L.-J. Xu, H. Yang, A. M. El-Zohry, B. Xin, S. Mitra, M. N. Hedhili, I. S. Roqan, O. F. Mohammed, Y. Han and O. M. Bakr, *Chem. Mater.*, 2019, **31**, 6642–6649.
- J. S. van der Burgt, J. J. Geuchies, B. van der Meer, H. Vanrompay, D. Zanaga, Y. Zhang, W. Albrecht, A. V. Petukhov, L. Filion, S. Bals, I. Swart and D. Vanmaekelbergh, *J. Phys. Chem. C*, 2018, **122**, 15706–15712.
- T. Xuan, X. Yang, S. Lou, J. Huang, Y. Liu, J. Yu, H. Li, K.-L. Wong, C. Wang and J. Wang, *Nanoscale*, 2017, **9**, 15286–15290.
- F. Yang, C. Wang, Y. Pan, X. Zhou, X. Kong and W. Ji, *Chin. Phys. B*, 2019, **28**, 056402.
- Z. Yang, Q. Xu, X. Wang, J. Lu, H. Wang, F. Li, L. Zhang, G. Hu and C. Pan, *Adv. Mater.*, 2018, **30**, 1802110.
- Y. Wang, M. Shi, Y.-Q. Chang, J.-P. Zhang and Y. Chan, *Nano Lett.*, 2018, **18**, 4976–4984.